Dynamic Simulator for a PEM Fuel Cell System With a PWM DC/DC Converter

Song-Yul (Ben) Choe, Jong-Woo Ahn, Jung-Gi Lee, *Student Member, IEEE*, and Soo-Hyun Baek

Abstract—Polymer electrolyte membrane (PEM) fuel cells typically have low voltage, high current, terminal characteristics that cannot accommodate common electric loads like electric motors or power utility grids. Thus, a dc/dc converter is required to boost the output voltage of these power systems. Furthermore, the terminal characteristics are dependent on loads and operating conditions of the fuel cell system. The continuously changing power demand of an electric load requires dynamically replenishing the air and fuel, by properly maintaining humidity in the cell and efficiently rejecting the heat produced. These factors present important challenges for the design of reliable and durable power systems. We present new dynamic models for a fuel cell system and a pulsewidth modulation dc/dc converter with associated controls and integration. The model for the system consists of three subsystems that include an PEM fuel cell stack, an air supply, and a thermal system. Four different controllers were designed to control the air, the coolant, and the output voltage of the converter, and to optimize the power flow between the fuel cell and the output capacitor. The integrated model with its controls was tested using a real-time simulator that reduced computational time and facilitated the analysis of the interactions between loads and the fuel cell components and also allowed the optimization of a power control strategy. The responses of a static and dynamic load show that the power controls proposed can coordinate two energy sources, resulting in improved dynamics and efficiency.

Index Terms—Air, polymer electrolyte membrane (PEM) fuel cell, pulsewidth modulation (PWM) dc/dc converter, temperature and power flow control.

NOMENCLATURE

A	Area (m^2).
C	Mass concentration or capacitor (kg/m^3, F).
Cp	Specific heat [$J/(kg \cdot k)$].
D	Switching on-duty period.
F	Faraday number (A·s/mol).
Fr	Frontal area (m^2).
h	Heat transfer coefficient [$W/(m^{2\circ}C)$].
i	Current density or current (A/cm^2, A).
J	Rotational inertia ($kg \cdot m^2$).
k	Specific heat ratio.
m	Mass (kg).
M	Molar mass(kg/mol).
N	Mole flux [$mol/(s \cdot m^2)$].
p	Pressure (atm, Pa).
P	Power (W).
Q	Heat transfer (J).
R	Resistance or gas constant [$\Omega, J/(kg \cdot K)$].
s	Entropy or balancing factor [$J/(mol \cdot K)$].
t	Thickness or time (m, s).
v, V	Voltages (V).
W	Mass flux [$kg/(s \cdot m^3)$].

Superscripts, Subscripts

an	Anode.
bl	Blower.
ca	Cathode.
cap	Capacitor.
con	Converter.
cv	Control volume.
DC	DC/DC converter.
FC	Fuel cell.
g	Gas.
i	Index.
membr	Membrane.
pl	Poles.
s	Stator.

Greek Symbols

γ	Ratio of the specific heat capacities.
ε	Porosity.
τ	Tortuosity or torque.
ρ	Density.
η	Efficiency.
ϕ	Flux linkage.
ω	Angular velocity.

I. INTRODUCTION

FUEL CELLS have great potential for the development as renewable power sources. In particular, the polymer electrolyte membrane (PEM) fuel cell technology is the best candidate among other fuel cell technologies including solid oxide fuel cell (SOFC), molten carbonate fuel cell (MCFC), phosphoric acid fuel cell (PAFC), and alkaline fuel cell (AFC), because of its low operating temperature, high-power density, and relatively short startup time. In addition, heat generated that is otherwise wasted can be reused for heating houses or other buildings, which increases the overall efficiency of the fuel cell power system.

An PEM fuel cell power system is comprised of an PEM fuel cell, a dc/dc converter with a capacitor, and a voltage impressed inverter that supplies power for the electric propulsion motors or a power grid. A typical mobile application of the PEM fuel cell with a propulsion motor is depicted in Fig. 1. This system

Fig. 1. Typical configuration of a PEM fuel cell powered system for automotive applications.

Fig. 2. Schematic diagram of a PEM fuel cell system.

includes a pulsewidth modulation (PWM) dc/dc converter that connects in series to the fuel cell power system and an inverter that drives the motor. Two controllers operate the fuel cell system and the motor, and the other one coordinates all components to produce torque demanded by the driver. Thus, the fuel cell power system consists of a stack of multiple cells assembled in series (or parallel) to generate electric power, and balance of the plants (BOPs) to supply reactants and to remove byproducts.

A single fuel cell is constructed by assembling different layers using bipolar plates (BP), gas diffusion layers (GDL), catalyst, and the membrane. The BPs and GDL allow the fuels to flow and provide paths for water flow and heat conduction. The membrane blocks electrons and allows transport of protons that are split by the reduction and oxidation processes at the catalyst material.

The electric power is generated from the chemical reaction of hydrogen and oxygen at the catalyst because of the change in the Gibb's free energy. Heat and water are released as byproducts of the reaction. The theoretical output voltage of a single cell is 1.23 V. In reality, the voltage of the cell drops the instant the current increases because of the augmented overpotentials at the electrodes and membrane. A high current leads to a rapid drop in voltage caused by flooding water that clogs the path of the reactants. Therefore, the fuel cell is a low-voltage energy source, where the amplitude drops nonlinearly as current increases. The maximum output voltage and current density of a single cell designed for mobile applications are 1.0 V and 1.0 A/cm^2, respectively. This yields a maximum power of approximately 136 W at an active area of size 516 cm^2.

The BOP is ancillary components that serve to supply fuels and remove byproducts. The BOP can be divided into four subsystems: 1) hydrogen, stored in a tank, which that is directly fed into the fuel cell, 2) oxygen, delivered by air via a compressor or blower and a humidifier, to maintain proper humidity in the cell, 3) heat produced, removed by a coolant circuit comprised of a heat exchanger, a coolant pump, and a reservoir, and 4) a load manager that coordinates all the aforementioned commands according to the load demand. The controls of the four subsystems
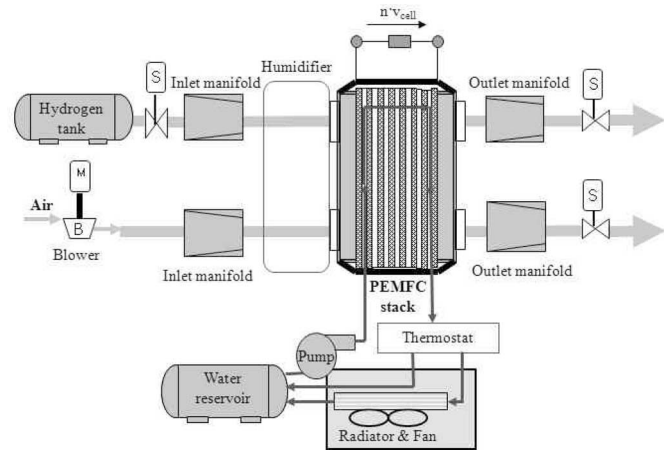
are very complex, and require a systematic design to obtain reliable operation of the fuel cell system as a power source.

Considering the electric characteristics mentioned earlier, the output voltage of the fuel cell should be transformed to a level of the dc bus voltage that is higher than the peak of the output ac line voltage. Generally, a booster PWM dc/dc converter is used to convert the fuel cell output voltage, and in principle, stores energy in an inductor by turning ON an active switch, which allows the transfer of energy to an output capacitor when the switch is turned OFF. The voltage at the capacitor can be kept constant, when the switching period is properly controlled, even at varying loads [1], [2]. The dc-link capacitor connected in parallel to the dc bus serves to deliver the current of a load that the fuel cell power system cannot otherwise supply dynamically because of the slow response time.

Understanding the effects of load currents on the supply of the fuels, rejection of heat, and removal of water are important for better performance and a durable power source. Modeling, controls, and simulation of an integrated PEM fuel cell power system described here enable dynamic analysis of the effects of electric loads on the individual layers of the fuel cell and other components of the fuel cell power system. Key components of the system include an PEM fuel cell stack, an air supply system and a thermal circuit, and an PWM dc/dc converter.

II. MODELING OF A FUEL CELL STACK, AIR SUPPLY, AND THERMAL CIRCUIT

Fig. 2 shows a block diagram of a fuel cell power system that includes a stack and four subsystems: the hydrogen supply, air supply, and water and thermal management systems. Assuming that the hydrogen flow rate is proportional to the airflow rate, the power of the stack can only be controlled by the flow rate of the air in the blower driven by an electric motor. In addition, it is assumed that the air is fully humidified and its temperature is the same as that in the stack. Heat produced by the stack is rejected by the coolants that exchange this heat with a radiator. Thus, the model for the entire fuel cell power system can be represented by a stack, an air supply system, a coolant circuit, and a dc/dc converter.

A. PEM Fuel Cell Stack

Models that describe the physical behavior of an PEM fuel cell have been developed from either empirical equations that were fitted to the curve of a specific polarization characteristic or the computational fluid dynamics (CFD) to solve for mass and charge transports in a cell. The former has been used here to design a controller for the air supply system. The dynamics of a fuel cell can be improved by reflecting the charging and discharging behavior of the double layer capacitor present at the interface between the electrodes and electrolytes [3]. However, the model does not fully represent the gas and temperature dynamics occurring through the flow paths and in the cell in relation to the current applied. The partial pressure drop along the pores in the GDL affects the net pressure exerted on the rate of the chemical reaction, and finally, increases the overpotential. In addition, a temperature rise facilitates to ease water removal and chemical reactions, which subsequently affects the output voltage of a cell.

By contrast, the CFD models have been employed to analyze the transport mechanism of the mass and charge and their spatial distributions only for a single cell. However, these are limited because they cannot represent the dynamic characteristics of a stack in conjunction with components of the BOP and a power system. Consequently, a new transient model considering key behaviors of an PEM fuel cell is needed.

The model proposed is derived from empirical equations and takes three major factors into account: the water balance in the membrane, the gas dynamics in the GDLs, and the temperature distribution in a cell.

1) Improvement of the Model for the PEM Fuel Cell Stack: A fuel cell is constructed by connecting individual cells in layers. The *I–V* characteristic is obtained by the difference between the open circuit voltage and the overpotentials that include the ohmic overpotential in the membrane, the activation overpotential in the catalyst on the cathode side, and the concentration overpotential. The mathematical relationship for a single cell is a function of physical parameters including the reactant partial pressure, temperature, current, and the water content in the membrane. The electrical output characteristic of the stack is assumed to be the same as that of a single cell multiplied by the cell number

$$v_{\mathrm{cell}} = E(p,T) - v_{\mathrm{act}}(p,T,i) - v_{\mathrm{ohm}}(i,\lambda_{\mathrm{membr}},T)$$
$$- v_{\mathrm{conc}}(p,T,i)$$
$$v_{\mathrm{stack}} = n \times v_{\mathrm{cell}}. \tag{1}$$

The dynamic behavior of a fuel cell system is influenced by various physical effects. The effect of the air mass flow and water on the dynamics is described by a lumped model, which shows a typical *I–V* characteristic of a single cell as well as its transient behavior. The transient behavior is dominated by the mass transport in the air delivery system [4]–[7]. It is possible to make further improvements in the dynamics by changing: 1) the water dynamics in the membrane, 2) the partial pressure drop in the GDL, and 3) the temperature variation.

Water content in the membrane determines the proton conductivity. The dynamics of the water content is described by

two effects, the electroosmotic driving force, or the different electrochemical potentials at the anode and cathode, and the diffusion caused by the water concentration gradient at the two boundaries. Considering that the water mass flows at the boundaries of the membrane layer, the dynamics of the water concentration in the membrane can be improved as follows [8]–[10]:

$$\lambda_{\mathrm{membr}} = \frac{C_{\mathrm{H_2O,mass}}/M_{\mathrm{H_2O}}}{\frac{\rho_{\mathrm{dry,membr}}}{M_{\mathrm{membr}}} - b \cdot C_{\mathrm{H_2O,mass}}/M_{\mathrm{H_2O}}}$$

$$\dot{m}_{\mathrm{water,membr}} = \frac{d(C_{\mathrm{H_2O,mass}} A_{\mathrm{cell}} t_{\mathrm{membr}})}{dt}$$
$$= W_{\mathrm{ele,membr,an}} - W_{\mathrm{ele,membr,ca}}$$
$$+ W_{\mathrm{diff,membr,an}} + W_{\mathrm{diff,membr,ca}} \tag{2}$$

where C is the mass concentration (in kilograms per cubic meter), M is the mole mass (in kilograms per mole), b is the membrane extension coefficient [9], ρ is the membrane dry density, and A_{cell} is the fuel cell area (in square meter).

The reactants entering the cell diffuse through the GDL before reaching the catalyst layer significantly affecting the overall dynamics of the reactants. This diffusion effect is described using the mass continuity (3) and the Stefan–Maxwell equations (4) [3]:

$$\frac{\varepsilon_g}{RT}\frac{\partial p_i}{\partial t} + \frac{\partial N_i}{\partial y} = 0 \tag{3}$$

$$\frac{\varepsilon_g}{\tau^2}\frac{\partial p_i}{\partial y} = \sum_{k=1}^{3}\frac{RT}{p_{\mathrm{ca}}D_{ik}}(p_i N_k - p_k N_i). \tag{4}$$

Hence, $i,k \in (1,3)$, where p_1 is the partial pressure of the oxygen, and $p_2 = p_{\mathrm{sat}}(T)$ and p_3 are the water vapor and the partial pressure of the nitrogen, respectively. The diffusion coefficients of $p_{\mathrm{ca}}D_{ik}$ include the cathode pressure of p_{ca}, summing the species partial pressures. The parameters τ and ε_g are constants describing the pore curvature of the GDL.

If a cell is assembled with cubical layers, where the thermophysical properties are isotropic and constant, then according to the energy conservation equation, the total energy change in a controlled volume is equal to the sum of energy exchange at the boundaries and the internal energy resources. In fact, the energy exchanges at boundaries occur because of three factors: 1) the mass flow into each volume; 2) the conduction heat transfer across the cell; and 3) the convection heat transfer occurring between bipolar plates with the coolant and the reactants. Thus, the thermal dynamic behavior can be described with the following energy conservation equation (5) [10]:

$$\sum Cp_i C_{i,\mathrm{mass}} A_{\mathrm{cell}} t_{\mathrm{cv}} \frac{dT_{\mathrm{cv}}}{dt} = \underbrace{\sum W_{\mathrm{in}} Cp_j (T_{\mathrm{in}} - T_{\mathrm{cv}})}_{\text{mass flow in}}$$
$$+ \underbrace{\dot{Q}_{\mathrm{conv}}}_{\text{convection heat transfer}} + \underbrace{\dot{Q}_{\mathrm{cond}}}_{\text{conduction heat transfer}} + \underbrace{\dot{Q}_{\mathrm{sou}}}_{\text{sources}} \cdot \tag{5}$$

Fuel Cell			Electrochemical Reation Model		
n	500	cells	P_0	1.0	bar
A_{fc}	645	cm^2	T_{ref}	353.15	K
Proton Conducting Model			E_{ref}	1.229	V [18]
b_{11}	0.5139	[6]	$A_{catl,eff}/A_{cell}$	f(I, T, P_{o2})	[18]
b_{12}	0.326	[6]	Thermal model		
b_2	350	[6]	H_{gas}	f(P, T)	[12]
n_d	f(C_{water})	[6]	Cp_{gas}	f(P, T)	[12]
D_w	f(T, C_{water})	[6]	?$_{gas}$	f(P, T)	[12]
Gas Tranport Model			Fr_{area}	1	m^2
Deff	f(P, T)	m^2/s [4]	M_{res}	5	kg
Psat	f(T)	[4]	hA	16.66	J/K
Geometrical data for layers [12]					
	Thickness m	Density W/mK	Heat conductivity J/kgK	Specific heat kg/m$^-$	
Coolant Channel	0.001	1400	30	935	
Plate	0.001	1400	52	935	
Gas Channel	0.001	1400	52	935	
GDL	0.0004	2000	65	840	
Catalyst layer	0.000065	387	0.2	770	
Membrane layer	0.000183	1967	0.21	1100	

The internal energy source is comprised of the entropy loss and the chemical energy necessary for protons to overcome the barrier of the overpotentials in both the catalyst layers (6). In addition, other losses are ohmic losses caused by the transport of electrons and protons in the cell [11]

$$\dot{Q}_{sou} = iA_{cell}\left(-\frac{T\Delta s}{4F} + v_{act} + iA_{cell}R_{elec}\right) \quad (6)$$

where Δs is equal to -326.36 J/(mol·K) [13], v_{act} is given in [18], and R_{elec} is the electrical resistance of the layers.

2) Parameters and Simulations: Table I shows that the parameters and reference data for the models chosen are partially empirical [3], [5], [11], [17]. In addition, the maximum voltage and current used for this study were 0.95 V and 0.95 A/cm^2, respectively.

Multirun simulations were conducted to investigate static and dynamic behavior of a single cell with fully humidified incoming reactants. The static behavior was analyzed by calculating the typical polarization at different temperatures, as shown in Fig. 3, and temperature distribution at a constant current load. The *I–V* characteristic was calculated from 60 °C to 80 °C in 10 °C steps. As the temperature increased, the removal of water was facilitated. The effects were highest at the high cell currents, where more water is produced. This result is comparable with the CFD analysis [12].

Fig. 4 shows the temperature distribution through the cell after 7 min. The catalyst layer on the cathode side exhibits a higher temperature than that on the anodic side because of the heat produced by the higher overpotential. Thus, the temperature distribution across the fuel cell was asymmetric. The maximum temperature difference between the catalyst at the cathode side and the coolant channel was 3 °C.
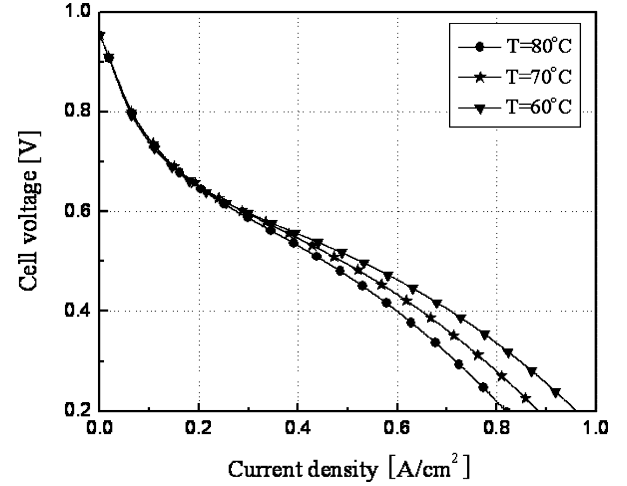

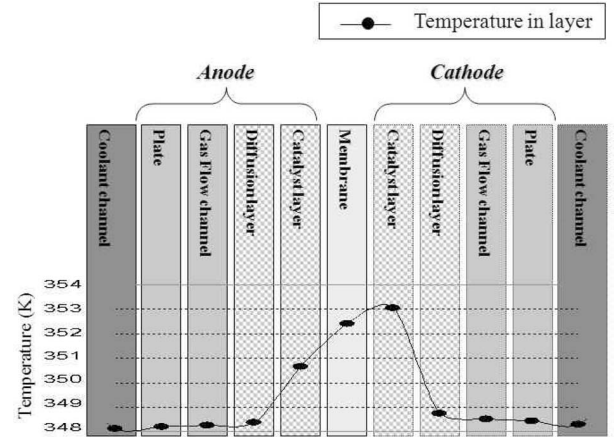Fig. 3. *I–V* curve for different cell working temperature: $P = 1.0$ bar.

Fig. 4. Temperature gradient in the cell 7 min after a start up (left to right: anode coolant channel to cathode coolant channel).

B. Air Supply System

The air supply system consists of a blower, a humidifier, and plumbings for the inlet and outlet. The outlet of the blower is connected to inlets of flow channels through a humidifier and pipes.

The blower is usually constructed with an impeller driven by an electric motor. The dynamic characteristic of the blower is mainly determined by the total inertia of the motor and the impeller and the torque produced by the motor. Hence, the torque produced by the motor $\tau_{bl,m}$ is a function of the stator resistance $R_{s,bl,m}$ (in ohm), magnetic flux constant $\Phi_{bl,m}$ (in volts second per radian), and the number of the poles $N_{bl,m,pl}$ with the stator voltage $V_{bl,m}$ (in volts) (8) [14]. Therefore, the flow rate W_{bl} (in kilograms per second), can be controlled by the voltage applied to the motor $V_{bl,m}$ (in volts)

$$\frac{d\omega_{bl}}{dt} = \frac{1}{J_{bl}}\left(\tau_{bl,m} - \frac{W_{bl}\Delta p_{bl}\eta_{bl,m}}{\eta_{bl}\rho_{amb}\omega_{bl}}\right) \quad (7)$$

$$\tau_{bl,m} = \eta_{bl,m}\frac{3}{2}\left(\frac{N_{bl,m,pl}}{2}\right)\left(\frac{\Phi_{bl,m}}{R_{s,bl,m}}\right)$$

$$\times \left[V_{bl,m} - \left(\frac{N_{bl,m,pl}}{2}\right)\Phi_{bl,m}\omega_{bl}\right] \quad (8)$$

where $\omega_{\rm bl}$: angular velocity (in radians per second), $J_{\rm bl}$: rotational inertia (in kilograms square meter), $\eta_{\rm bl,m}$: motor efficiency, $P_{\rm bl}$: pressure (in pascals), and $\rho_{\rm amb}$: density (in kilograms per cubic meter).

The blower parameters were derived from the characteristic data and specifications delivered by Phoenix Analysis & Design Technologies (PADT) [15], which included both the flow parameter and overall efficiency versus the head parameter. The behavior of an impeller can be described as follows [17]:

$$W_{\rm bl}$$
$$= \begin{cases} \omega_{\rm bl}[-20.581\,(p^*)^2 - 1.4415 \times 10^{-3} p^* + 4.1333 \times 10^{-5}] \\ \text{where, } p^* \le 9 \times 10^{-4} \,{\rm Pa \cdot s^2/rad^2} \\ \text{otherwise, } \omega_{\rm bl}\left[-1.7973 p^* + 1.640 \times 10^{-3}\right] \end{cases}$$
$$(9)$$

$$\eta_{\rm bl} = -2.8831 \times 10^{13} \left(\frac{W_{\rm bl}}{\omega_{\rm bl}}\right)^3 + 9.5115 \times 10^8 \left(\frac{W_{\rm bl}}{\omega_{\rm bl}}\right)^2$$
$$+ 1.3087 \times 10^4 \left(\frac{W_{\rm bl}}{\omega_{\rm bl}}\right) + 0.17945 \qquad (10)$$

where $p*$ is $(p_{\rm ca} - p_{\rm amb})/\omega_{\rm bl}^2$.

Inlet and outlet manifold pressures are described by the mass conservation equation

$$\dot{p}_{\rm im} = \frac{\gamma R_a}{V_{\rm im}} \left(W_{\rm bl} T_{\rm bl} - W_{\rm im,out} T_{\rm im}\right) \qquad (11)$$

$$\dot{p}_{\rm om} = \frac{R_a T_{\rm om}}{V_{\rm om}} \left(W_{\rm ca,out} - W_{\rm om,out}\right) \qquad (12)$$

where γ is the ratio of the specific heat capacity of gas.

C. Thermal Circuit

A thermal system rejects excess heat produced by losses in the stack. Major components of the circuit are a radiator for heat exchange with the ambient air, a fan to increase the effectiveness of the heat convection and radiation, and a water reservoir to store and thermally insulate the coolants. Finally, a pump supplies the coolant to the stack. The models for these components are derived from the principles of heat transfer. Kroger [16] proposed a heat transfer coefficient $h_{\rm rad}$ (in kilowatts per square meter per degree Celsius), and pressure drop P_r (in kilopascals) of a radiator as a function of the airflow rate $W_{\rm air}$ (in kilograms per second):

$$h_{\rm rad} = -1.4495 W_{\rm air}^2 + 5.9045 W_{\rm air} - 0.1157 \qquad (13)$$
$$p_r = (326.12 W_{\rm air} - 75.396) + 101.325. \qquad (14)$$

If the heat of the coolant is transferred to the radiator without any losses, the heat capacity of the coolant is identical to the radiator. Thus, the outlet temperature of the coolant can be expressed as a function of the radiator geometry, the temperature drop between the inlet and outlet, and the heat convection caused by the temperature difference between the ambient and the outgoing air temperature [16]

$$T_{c,\rm rad,out} = T_{c,\rm rad,in} - 0.5 \left(\frac{Fr_{\rm area}\,(T_{c,\rm rad,in} - T_{\rm amb})\,h_{\rm rad}}{W_c C p_c}\right) \qquad (15)$$

where $Fr_{\rm area}$ denotes the frontal area (in square meter) of the radiator and $T_{c,\rm rad,in}$ denotes the stack outlet temperature of the air. The electric power for the fan can be calculated according to a thermal dynamic relationship between the pressure drop and airflow rate [11]

$$P_{\rm fan} = \frac{1}{\eta_{\rm elec}\eta_{\rm fan}} \left(W_{\rm air} C p_{\rm air} T_{\rm amb} \left(P_r^{\left(\frac{k-1}{k}\right)} - 1\right)\right) \qquad (16)$$

where $P_{\rm fan}$ denotes the electric power (in watts) of the fan and k is the specific heat ratio.

The reservoir should be thermally insulated after the heat exchange occurs at the radiator by convection. The variation of the heat in the reservoir is the sum of the heat that the coolant carries and the heat exchanged with the ambient air. Accordingly, the outlet temperature at the end of a given time interval can be expressed by the equation [11]

$$T_{\rm res} = T_{\rm res,p} - \frac{\Delta t}{m_{\rm res} C p_{\rm res}} (W_c C p_c (T_{\rm res,p} - T_{\rm res,in})$$
$$+ hA(T_{\rm res,in} - T_{\rm amb})) \qquad (17)$$

where $T_{\rm res}$ is the outlet temperature of a reservoir at the end of a time step (in kelvin), $T_{\rm res,p}$ is the temperature of the reservoir at the previous time step (in kelvin), Δt is the time interval (in seconds), $m_{\rm res}$ is an equivalent mass of the coolant in the control volume (in kilograms), and $T_{\rm res,in}$ is the temperature of the coolant entering the reservoir (in kelvin), and hA is the heat transfer from the reservoir to ambient air.

The coolant pump should deliver the coolants from the reservoir and the stack to the radiator. Provided that all heat energy generated in the stack is completely transferred to the coolant, the mass flow rate of the coolant is expressed by the relationship with the heat source

$$W_c = \frac{\dot{Q}_{\rm sou}}{C p_c \Delta T}. \qquad (18)$$

D. Control of the Air and Coolant Flow Rate

Fig. 5 depicts a block diagram for the controls that includes two conventional PI controllers for controlling the air and the coolant flow rates.

Pukrushpan *et al.* [9] proposed different control strategies for the air supply system. The air supply control is able to maintain the optimal oxygen excess ratio and prevent oxygen starvation that might occur during abrupt changes of the load current. Hence, the oxygen excess ratio is defined as the rate of oxygen supplied to that consumed. Two control strategies, a static feedforward (sFF) and a static feedback (sFB), were designed for the air supply system and are presented in Fig. 7.

The sFF principle requires a polynomial that interpolates map data. This assures that an optimal relationship between the stack current and the motor voltage of the blower and helps to maintain
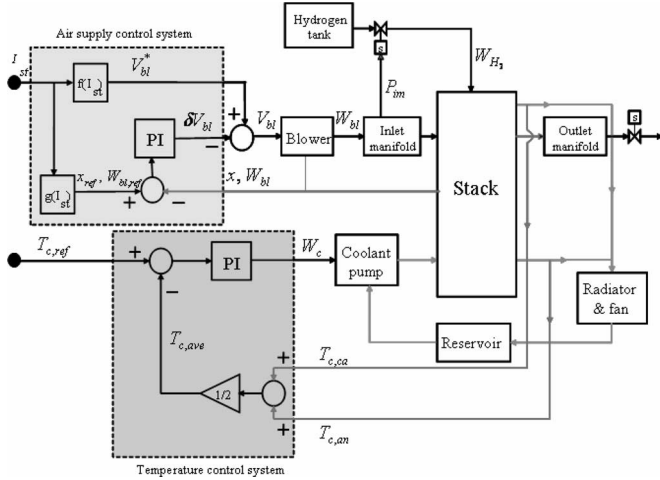
Fig. 5. Block diagram for the air and coolant flow control.

Fig. 6. Effect of the weighting factor on the recovery behavior of the oxygen excess ratio. (a) Q_I. (b) Q_z.

the oxygen excess ratio at 2, provided that the airflow of the blower can be controlled by the motor voltage.

According to simulations, the sFF showed excellent dynamic behavior at the rejection of the disturbance, but still exhibited a steady-state error. The errors were removed by employing a feedback controller as shown in Fig. 5. The sFB principle requires compensation of the blower motor voltage by the use of an PI controller that amplifies the deviation between the actual state values and the state values at a given stack current used for the sFF. In fact, the stack with the air supply system can be described by differential equations, which include nonlinear terms. Therefore, the nonlinear equations are linearized at an operating point where the stack current $w^o = I_{st} = 258$ A, the blower motor voltage $u^o = V_{bl}^{opt} = 118$ V, and the oxygen excess ratio $\lambda_{O_2}^{opt} = 2$. As a result, linear equations are obtained and expressed with the following general form (19):

$$\delta\dot{x} = A\delta x + B_u\delta u + B_w\delta w$$
$$\delta y = C_y\delta x + D_{yu}\delta u + D_{yw}\delta w$$
$$\delta z = C_z\delta x + D_{zu}\delta u + D_{zw}\delta w \qquad (19)$$

where δ denotes the derivative operator at an operating point. Thus, the variables of the fuel cell system can be defined as

$x = [m_{O_2} \ m_{H_2} \ m_{N_2} \ \omega_{bl} \ p_{im} \ m_{im} \ m_{w,an} \ p_{om}]$ (states)

$x = [m_{O_2} \ m_{H_2} \ m_{N_2} \ \omega_{bl} \ p_{im} \ m_{im} \ m_{w,an} \ p_{om}]$ (control variable)

$x = [m_{O_2} \ m_{H_2} \ m_{N_2} \ \omega_{bl} \ p_{im} \ m_{im} \ m_{w,an} \ p_{om}]$ (disturbance)

$y = [W_{bl} \ p_{im} \ V_{st}]$ (output)

$z = [P_{net} \ \lambda_{O_2}]$ (performance variables).

The matrix values of the linearized system including $A, B_u, B_w, C_y, D_{yu}, D_{yw}, C_z, D_{zu},$ and D_{zw} are listed in the Appendix. The units used for state and output variables are: m (in grams), p (bar), ω (kilo revolutions per minute), W (in grams per second), P (in kilowatt), V (in volts) and I (ampere). The gains of the PI controller for the sFB were optimized by using the linear quadratic regulator (LQR). A new state variable q was
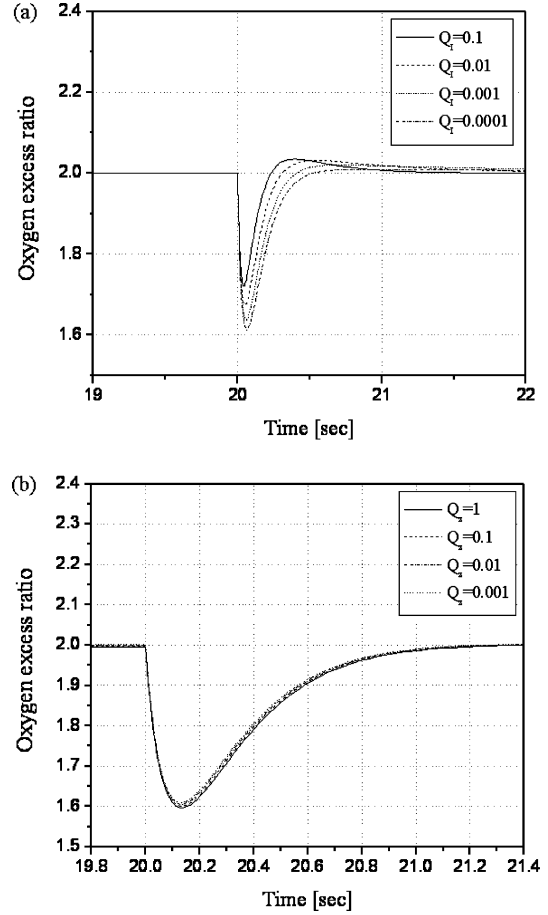
defined, which represents the error of the airflow rate resulting from the deviation of the states. Thus, the PI controller should reflect the error of the flow rates along with the deviation of the state variables

$$q = W_{bl} - W_{bl}^{ref}. \qquad (20)$$

The final motor voltage can be obtained by the following equation with a control input $u(= V_{bl})$:

$$u = u^* - K_p\Delta x - K_I q \qquad (21)$$

where Δx denotes the state errors, u^* the optimal blow voltage to achieve the desired airflow rate, and K_p and K_I denote the gains for the controller.

The gains for the PI controller were optimized by using the LQR. If the cost function J (22) is a minimum value, the gains become optimal

$$J = \int_0^\infty \left(\delta z_2^T Q_z \delta z_2 + q^T Q_I q + \delta u^T R \delta u \right) dt \qquad (22)$$

where Q_z and Q_I represent the weighting factors amplifying the errors of the control objects, while the other weighting matrix R is used to suppress the effects of the manipulating variable. The response of the oxygen excess ratio to different weighting factors is shown in Fig. 6.
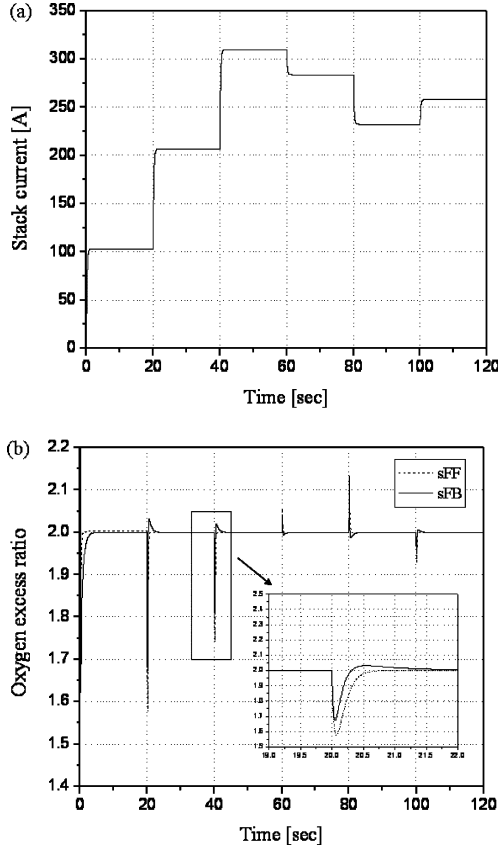
Fig. 7. Comparison between sFF and sFB at a constant temperature of the stack. (a) Current. (b) Oxygen excess ratio.

According to studies, the weighting factor Q_I only influences the flow rate error q, and the integrator gain in the second term of the cost function. When Q_I increases, the overall influence of the second term in the cost function becomes larger. Therefore, the rest terms in the function become smaller at a minimal value of the function. In fact, the variable δz_2 is a function of the state variables $C_z \delta x$. As a result, the decreased δz_2 leads to an increase in the error that cannot be removed by the proportional controller. Additionally, the influence of the integrator becomes larger. Consequently, the dynamic response of the recovery behavior of the oxygen excess ratio becomes faster, and the oxygen excess ratio is slightly greater than 2 before achieving a steady state.

Conversely, the weighting factor Q_z does little to improve the transition behavior. The optimum values of the weighting factors are determined with $Q_z = 1$ and $Q_I = 0.01$, which results in the following gains for the PI controller:

$$K_p = [-1.1060 \times 10^5 \quad 0 \quad -1.2636 \times 10^5 \quad 20.717$$
$$2.7681 \times 10^3 \quad -0.0019 \quad 0 \quad 33.5587]$$
$$K_I = -3.1623. \tag{23}$$

Fig. 7 shows a comparison of responses of the sFF and the sFB on a multiple-step current, where the sFB improved the rejection dynamics on the disturbance the instant the step current changed. In addition, the excursion of the oxygen excess ratio was reduced with the sFB.

All previous designs assumed that the working temperature of the cell was constant. However, the temperature in the stack varies because of the heat produced by irreversible energy occurring in the chemical reactions, and Joule's losses associated with charge transport. The stack constructed with different layers and thermal characteristics can be approximated with a lumped model that has a thermal mass with a thermal capacity. Then, the variation of the temperature in the stack is equal to the sum of all the source terms in the stack and the heat exchanged with the coolants, provided that the heat exchange by radiation is negligible and the coolant temperature on the anode and cathode are equal to each other. As a result, a lumped thermal model for designing a temperature controller can be obtained:

$$m_{\text{st}} C p_{\text{st}} \frac{dT_{\text{st}}}{dt} = \dot{Q}_{\text{sou}} - W_c C p_c \left(T_{\text{st}} - T_{c,\text{in}} \right) \tag{24}$$

where m_{st} is the heat mass of the stack, Cp_{st} and Cp_c is the specific heat (in joules per kilogram per kelvin), W_c is the coolant flow rate (in kilograms per second) as a control variable, and $\dot{Q}_{\text{sou}}$ is the internal energy source (in joules per second) that is a function of the current generated.

The aforementioned equation includes a nonlinear item coupled with the coolant flow rate and the coolant temperature at the stack outlet ($T_{c,\text{out}}$), which can be expanded according to the Taylor series and results in a linear equation at an operating point $T_{c,\text{out}} = 77\,^\circ\text{C}$ and $W_c = 0.583$ kg/s along with the same stack current and voltage used for the air supply system.

Transfer function of the linearized equation transformed to the Laplace domain yields the following equation for the stack temperature with respect to the coolant flow rate:

$$\frac{T_{\text{st}}\left(s\right)}{W_c\left(s\right)} = \frac{Cp_c T_{c,\text{in}}^o}{\left(m_{\text{st}} C p_{\text{st}} s + W_c^0 C p_c \right)}. \tag{25}$$

This equation is the first order of an ordinary differential equation, which can be easily controlled by a classic PI control.

$$G_c\left(s\right) = K_p + \frac{K_I}{s}. \tag{26}$$

The two gains of the PI controller are chosen by the bandwidth of the closed loop that should be five times higher than the time constant of the thermal system and a damping ratio of 0.7. The resulting gains were $K_p = 0.3068$ and $K_I = 0.024$.

When the load current varied abruptly, the temperature in the stack increased, particularly in the catalyst as shown in Fig. 8, even though the temperature in the coolant channel follows the set point. The temperature in the catalysts is not measurable. Therefore, the actual temperature of the stack necessary for the controls is assumed to be the average value of the outlet of the anode and the cathode side. The reference temperature of the stack was set to 77 °C. It should be noted that the temperature in the catalysts on the cathode side increased by about 3–8 °C over the average temperature of a stack due to the losses, which depend upon the characteristics of the load current drawn. When the temperature varied, the oxygen excess ratio set at a constant temperature deviated from the optimal point because of the
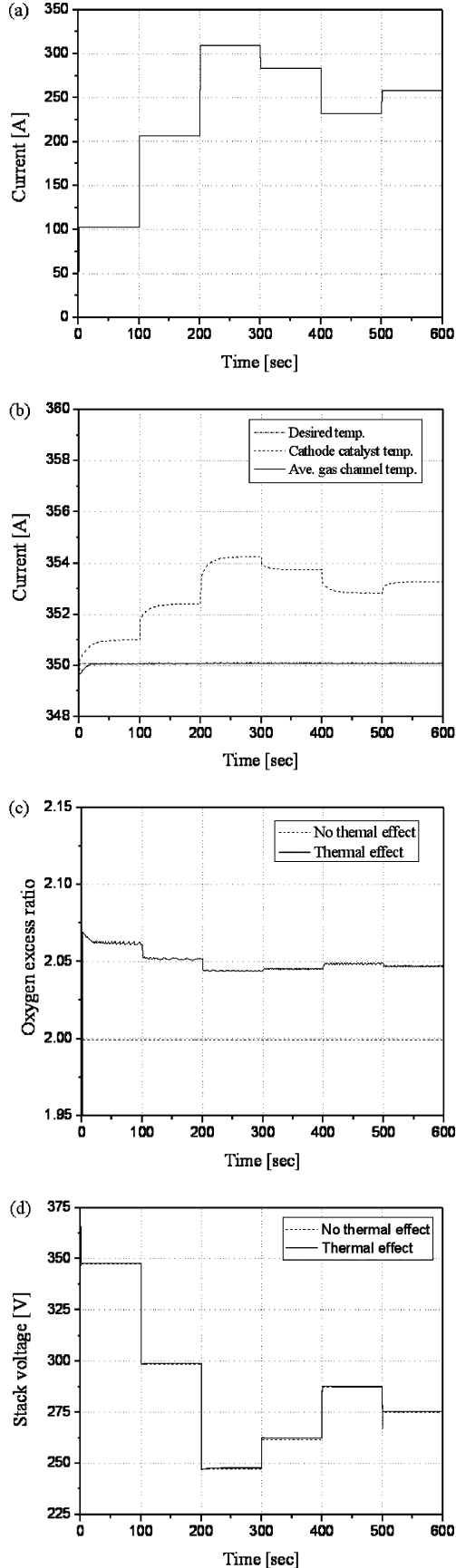
Fig. 8.   (a) Step current. (b) Catalyst and gas temperature. (c) Oxygen excess ratio. (d) Stack voltage.

influence of the coolant temperature on the air mass in the gas flow channel. At a given profile of the load current, the oxygen excess ratio was positively offset and with a value of 2.05.

In general, the oxygen excess ratio varied inversely as the current increased or decreased. At an increased current, more heat was generated in the catalyst and the temperature in each layer increased. In fact, the temperature of the coolant remained the same as the reference value. Therefore, the temperature in the flow channel increased as the load current increased, which resulted in a rise in the partial pressure in the gas channel. Consequently, the mass of the air is less and the associated oxygen excess ratio becomes lower. Likewise, the oxygen excess ratio gets higher as the current decreases.

III. DC/DC CONVERTER

As shown in Fig. 1, the PWM dc/dc converter operates as a booster that can be described by two state equations (27) and (28), provided that the converter operates in conduction mode, and the current in the inductor flows continuously. In addition, all losses are negligible [19]–[21]:

$$\frac{dv_{DC}}{dt} = \frac{1}{C}i_{cap} = \frac{1}{C}(1-D)i_{FC} - \frac{v_{DC}}{CR_{load}} \qquad (27)$$

$$\frac{di_{FC}}{dt} = \frac{1}{L}\left(v_{FC} - (1-D)v_{DC}\right) = \frac{1}{L}(v_{FC} - v_1) \quad (28)$$

where v_1 denotes the average voltage at the lower switch during the PWM period, D the switching onduty period, v_{FC} the output voltage of the fuel cell system, and v_{DC} the output voltage of the converter.

The input power of the converter $P_{FC} = i_{FC}v_{FC}$ is equal to the output power of the converter $P_{con} = i_{con}v_{DC}$. The current at the output and the capacitor can be described as follows:

$$i_{con} = \frac{P_{FC}}{v_{DC}} = \frac{v_{FC}i_{FC}}{v_{DC}} \qquad (29)$$

$$i_{cap} = i_{con} - i_{load} \qquad (30)$$

$$i_{con} = \frac{v_{FC}i_{FC}}{v_{DC}} - i_{load}. \qquad (31)$$

The aforementioned equations represent a second-order linear system with two state variables, the dc output voltage and the fuel cell current i_{FC}. The corresponding block diagram for the dc/dc PWM converter is shown in Fig. 9.

Two PI controllers are used for the current and voltage loop in a cascade configuration. In addition, a feedforward controller is employed to increase the dynamic response of the current loop at a sudden change of the reference voltage. The feedforward controller captures any static error between the reference of the output voltage and the input voltage and increases the capacitor current. The equations for the two controllers are given as

$$v_1^* = -\left(k_{p1} + \frac{k_{i1}}{s}\right)\left(i_{cap}^* - i_{cap}\right) + v_{FC} \qquad (32)$$

$$i_{cap}^* = \left(k_{p2} + \frac{k_{i2}}{s}\right)\left(v_{DC}^* - v_{DC}\right). \qquad (33)$$
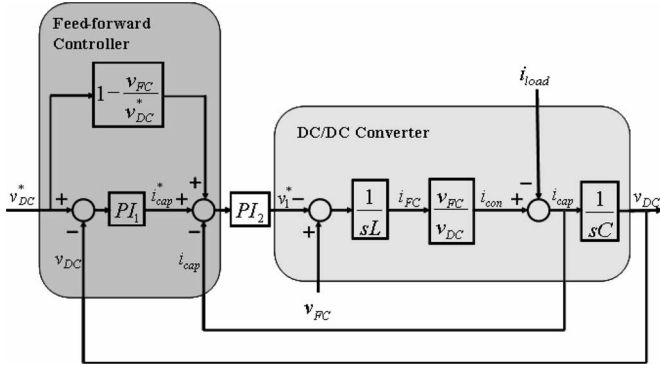
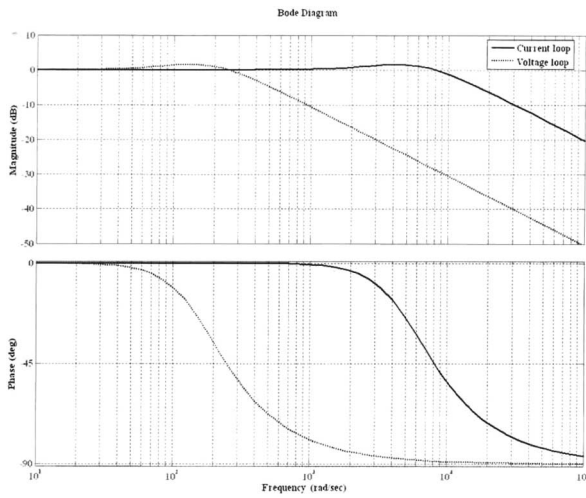Fig. 9. Control block diagram for the PWM dc/dc converter.

Fig. 10. Bode plot of the transfer function of the current loop (solid line) and the voltage loop (dash line).

The gains of the current controller are determined at an operating point duty ratio $D = 0.5$, where ω_n of the resulting poles should be located in the negative half plane and the damping coefficient ξ should be $0.707 < \xi < 1$. The transfer function of the current loop is given as follows:

$$G(s)_{\text{current}} = \frac{K_{p2}(1-D)s + K_{i2}(1-D)}{Ls^2 + K_{p2}(1-D)s + K_{i2}(1-D)} \quad (34)$$

where the values designed for the current loop were $\xi = 0.8480$, $\omega_n = 5773$ rad/s, $K_{p2} = 4.7$, and $K_{i2} = 160\,\text{s}^{-1}$. The Bode plot is depicted in Fig. 10. The crossover frequency of the current loop was 1.44 kHz. The phase and magnitude margin were $40°$ and 25 dB, respectively.

The transfer function of the voltage loop is shown in (35), where the inner current loop is approximated with a unity gain

$$G(s)_{\text{voltage}} = \frac{K_{p1}s + K_{i1}}{Cs^2 + K_{p1}s + K_{i1}}. \quad (35)$$

Like the current loop, the gains of the controllers were determined by the following values: $\xi = 0.8285$, $\omega_n = 178$ rad/s, $K_{p1} = 0.6$, and $K_{i1} = 6.4\,\text{s}^{-1}$. The crossover frequency of the

voltage loop was 35 Hz. The phase and gain margin were $45°$ and 40 dB, respectively (see Fig. 10).

IV. POWER CONTROL OF THE PEM FUEL CELL SYSTEM WITH THE DC/DC CONVERTER

The objective of power flow control is to accurately and dynamically supply power, maximizing overall system efficiency, while maintaining the dc voltage level at the capacitor, which should not interfere with the performance of the motor drive system. There are two energy sources available that can be combined to increase the overall efficiency [22], [23]. The total power that the system can supply is the sum of the power that the dc capacitor can deliver and the power generated by the stack. This can be expressed mathematically if the ratio of both powers is defined as a new variable s; then, the total power can be expressed as follows:

$$\begin{aligned} P_{\text{total}}(t) &= P_{\text{FC}}(t) + P_{\text{DC}}(t) \\ &= sP_{\text{DC}}(t) + P_{\text{DC}}(t) \\ &= (s+1)P_{\text{DC}}(t). \end{aligned} \quad (36)$$

The variable s determines a factor responsible for the power split between the fuel cell and the capacitor, which can be controlled according to the efficiency and the power supplied by the capacitor.

When the derivative of the dc voltage is negative, the capacitor must be recharged from the stack. Otherwise, the dc capacitor will supply only a certain amount of power to the load. Then, the reference power for the fuel cell stack is adjusted by a new value of the variable s, which is determined by considering an efficiency map of the stack stored. As a result, a new reference for the stack current I_{FC}^* is generated by division of the dc power and the output voltage of the stack, which is expressed as follows:

$$P_{\text{DC}}^* = (sx(t) + s(x(t) - 1))\,P_{\text{DC}}$$

$$x(t) = \begin{cases} 0: & \dfrac{v_{\text{DC}}}{dt} < 0 \\ 1: & \dfrac{v_{\text{DC}}}{dt} > 0 \end{cases} \quad (37)$$

$$I_{\text{FC}}^* = \frac{(1 + s(t))P_{\text{DC}}^*}{V_{\text{FC}}}. \quad (38)$$

V. INTEGRATION AND SIMULATION

The models developed were implemented with the MATLAB/Simulink/Simpower software package, which was complied for a real-time system that allows for significant reduction of the computational time. The fuel cell system was connected to the converter by using a voltage source control block that was available in the software package. The current at the inductor was set equal to that of the reference current for the stack, which controls the low rate and pressure of the supplying air. However, the fuel cell system and the dc/dc converter, switching at 20 kHz, have different time constants. Thus, it takes days to complete a simulation under these conditions. Therefore, a commercial real-time simulator (RT-LAB, provided by

TABLE II
SIMULATION PARAMETERS FOR THE PWM DC/DC CONVERTER

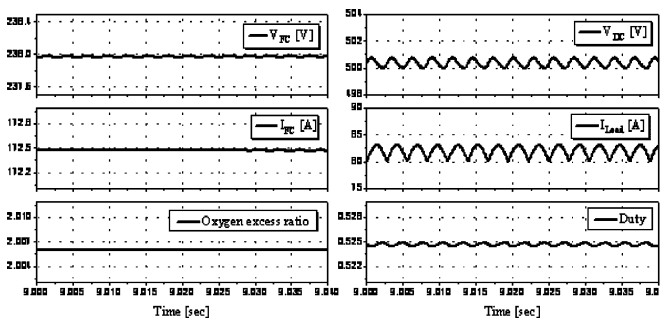| Swiching frequency	20	kHz
V_{DC}	500	V
C	1500	μF
C_{in}	350	μF
L	240	μH
R_{load}	6.25-62.5	O
IGBT forward voltage	1	V
IGBT OFF current tail time	4×10^{-6}	sec
IGBT ON	0.017	sec
Diode ON	0.015	O
Diode forward toltage	0.8	V
Calcculation step size	1×10^{-6}	sec

Fig. 11.   Voltage and current waveforms at a mixed load ($V_{dc} = 500$ V).

OPAL-RT) was used as a platform for implementation of the models. In fact, RT-LAB offers two attractive techniques. A new block for a power transistor was developed for this application and a parallel set of codes were developed by using transmission control protocol (TCP)/IP, which drastically reduced the computational time. In order to run the models on the simulator, all numerical integrations were modified for a fixed step. The dc/dc converter and the PEM fuel cell model were divided into two system blocks. Each of the blocks was assigned to a processor that calculated the model and exchanged data with other processors. A third processor coordinated the two processors, and managed the storage and retrieval of the simulation results in real time. The studies presented were developed on the basis of an operating point, where the dc voltage of the fuel cell stack was approximately 250 V with an output power of 40 kW. The parameters used for the simulation are summarized in Table II.

Simulations were carried out at a static and dynamic load, where an ac and a step-like current were applied. The dc voltage at the capacitor fluctuated with a frequency that was six times higher than the frequency of the voltage and current of a load. Fig. 11 shows the waveforms of the dc voltage, dc load current, the duty cycle of the PWM dc/dc converter, the output voltage, the current of the fuel cell power system, and the oxygen excess ratio. The frequency of the impressed voltage for the motor was assumed to be 60 Hz, and the resulting harmonic frequency of the dc voltage was 360 Hz. Accordingly, the modulation grade for the PWM signal followed the variation of the voltage at the capacitor and the corresponding oxygen excess ratio.
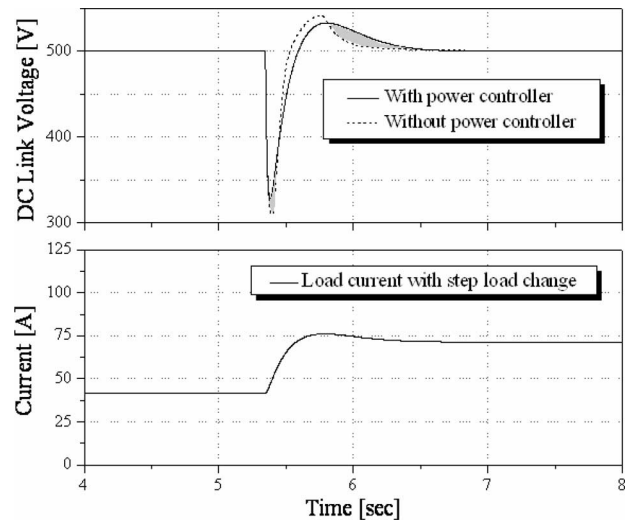

Fig. 12.   Dynamic response of the dc voltage at current load.
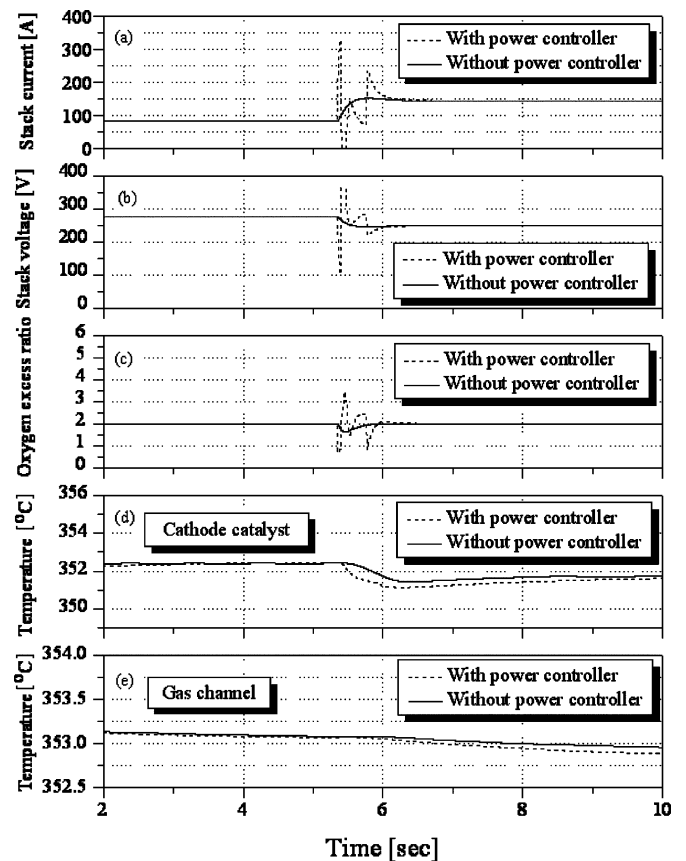

Fig. 13.   Dynamic response of the fuel cell power system at a step load with the power control.

Fig. 12 shows the effects of the power control when the load current changed dynamically from 40 to 70 A. The gray areas represent the contribution of the energy stored in the capacitors. When a load was applied, the voltage at the capacitor dropped and the stack immediately reacted to refill the voltage gap by supplying the current. At the same time, the capacitor was being charged and the voltage at the capacitor increased. Thus, the

supply of power from the stack was reduced to operate the stack more efficiently. This switching mechanism was repeated until the voltage achieved the set steady state.

Fig. 13 shows the simulated results for the current, voltage, oxygen excess ratio, and the temperature in the cathode catalysts and the gas flow channel of a fuel cell stack. When a step-like current was applied, the current and voltage of the stack followed the load changes with a time constant determined by the air supply system. When the new power controller was employed, the reference values for the stack current and voltage were continuously shifted to obtain an efficient operating point. Accordingly, the current, voltage, and oxygen excess ratio all varied dynamically. However, the temperature rise in the catalysts during the transition was slightly lower than that without the power controller, which indicates reduced losses in the cell [see Fig. 13(c)]. Also, the temperature in the gas flow channel was lower even while considering the increased load.

VI. CONCLUSION

The modeling and controls of an PEM fuel cell power system that includes a stack with an air supply system and thermal circuit, and an PWM dc/dc converter were presented. Simulations of the integrated model were performed using a commercial real-time simulator, RT-LAB. The integration of the components of the model revealed a number of ways to analyze: 1) the effects of electric loads on the system and its components; 2) study design parameters, particularly the realistic characteristics of the fuel cell stack; and 3) the dynamics of the air supply and the thermal system with all the associated controls. A static and a dynamic electric load were applied to the system and their interrelated responses were analyzed. The major contributions of this paper are summarized as follows.

1) The current dynamic model of the stack used for controlling a power system can be improved by considering the water balance at the boundary of the membrane, diffusion effects in the GDL, and temperature variations.
2) The oxygen excess ratio is inversely influenced by the load profile because of the change of partial pressure in the gas flow channel.

3) The dynamics and efficiency can be improved by using the energy stored in the capacitor that continuously shifts the operating point of the stack to a highly efficient region.
4) Real-time simulation with the fuel cell stack and the dc/dc converter reduces the computational time by two orders of magnitude, which provides a new way to develop a real-time dynamic power simulator that facilitates interacting effects between electric loads and individual components of the system.

In the future, we plan to focus on: 1) validation of the models, 2) integration of the model for an electric machine, 3) improving the temperature control to minimize the temperature rise in the catalyst, 4) compensation of the temperature effect on the oxygen excess ratio, and 5) advanced power management, taking into account the fuel cell dynamics and efficiency.

APPENDIX

Values for the system matrices used in (19) are listed here and at the bottom of the page:

$$B_u^T = [0 \quad 0 \quad 0 \quad 2.6578 \times 10^4 0 \quad 0 \quad 0 \quad 0]$$

$$B_w^T = [-8.291 \times 10^{-5} \quad -1.036 \times 10^{-5} \quad 0 \quad 0 \quad 0 \quad 0$$
$$- 1.741 \times 10^{-5} \quad 0]$$

$$C_v = \begin{bmatrix} 0 & 0 & 0 & 57038 & -876.6 & 0 & 0 & 0 \\ 0 & 0 & 0 & 0 & 1 & 0 & 0 & 0 \\ 267.3 & 5694 & 1083 & 0 & 0 & 0 & 9884 & 0 \end{bmatrix}$$

$$D_{yu} = \begin{bmatrix} 0 \\ 0 \\ 0 \end{bmatrix} D_{yw} = \begin{bmatrix} 0 \\ 0 \\ -0.3854 \end{bmatrix}$$

$$D_{zu} = \begin{bmatrix} -0.169 \\ 0 \end{bmatrix} D_{zw} = \begin{bmatrix} 0.1802 \\ -0.01055 \end{bmatrix}.$$

$$A = \begin{bmatrix} -4.633 \times 10^4 & 0 & -5.292 \times 10^4 & 0 & 1.154 \times 10^3 & 0 & 0 & 18.91 \\ 0 & -2.177 \times 10^4 & 0 & 0 & 2.535 & 0 & -2435 & 32.18 \\ -1.549 \times 10^5 & 0 & -1.77 \times 10^5 & 0 & 3798 & 0 & 0 & 124.5 \\ 0 & 0 & 0 & -11.3 & 3.518 \times 10^4 & 0 & 0 & 0 \\ 6.041 \times 10^6 & 0 & 6.901 \times 10^6 & 0 & -1.53 \times 10^5 & 0.236 & 0 & 0 \\ 9.87 \times 10^7 & 0 & 1.128 \times 10^8 & 0 & -2.501 \times 10^6 & 0 & 0 & 0 \\ 0 & -1.281 \times 10^5 & 0 & 0 & 18.61 & 0 & -1.437 \times 10^4 & 185.6 \\ 6.641 \times 10^5 & 0 & 7.587 \times 10^5 & 0 & 0 & 0 & 0 & -1.707 \times 10^4 \end{bmatrix} \tag{*}$$

$$C_z = \begin{bmatrix} 893 & 1928 & 366.8 & 0.276 & 0 & 0 & 3347 & 0 \\ -2.13 \times 10^6 & 0 & -2.433 \times 10^6 & 0 & 53920 & 0 & 0 & 0 \end{bmatrix} \tag{**}$$

REFERENCES

[1] N. Mohan, T. M. Undeland, and W. P. Robbins, *Power Electronics, Converters, Applications and Design*.   Toronto, ON, Canada: Wiley, 1995.

[2] H. Rudnick, J. Dixon, and L. Moran, "Delivering clean and pure power," *IEEE Power Energy Mag.*, vol. 1, no. 5, pp. 32–40, Sep./Oct. 2003.

[3] M. Ceraolo, C. Miulli, and A. Pozio, "Modeling static and dynamic behavior of proton exchange membrane fuel cell on the basis of electrochemical description," *J. Power Sources*, vol. 113, pp. 131–144, 2003.

[4] T. V. Nguyen and R. E. White, "A water and heat management model for proton-exchange-membrane fuel cells," *J. Electrochem. Soc.*, vol. 140, no. 8, pp. 2178–2186, 1993.

[5] T. E. Springer, T. A. Zawodzinski, and S. Gottesfeld, "Polymer electrolyte fuel cell model," *J. Electrochem. Soc.*, vol. 138, no. 8, pp. 2334–2342, 1993.

[6] J. H. Le and T. R. Lalk, "Modeling fuel cell stack systems," *J. Power Sources*, vol. 73, pp. 229–241, 1998.

[7] L. Guzzella, "Control oriented modeling of fuel-cell based vehicles," presented at the NSF Workshop Integr. Model. Control Autom. Syst.. Santa Barbara, CA, 1999.

[8] J. C. Amphlett, R. M. Baumert, R. F. Mann, B. A. Peppley, P. R. Roberge, and A. Rodrigues, "Performance modeling of the Ballard Mark IV solid polymer electrolyte fuel cell," *J. Power Sources*, vol. 49, pp. 349–356, 1994.

[9] J. T. Pukrushpan, H. Peng, and A.G. Stefanopoulou, "Simulation and analysis of transient fuel cell system performance based on a dynamic reaction flow model," presented at the IMEXE 2002 ASME Int. Mech. Eng. Congr. Expo., New Orleans, LA.

[10] Y. Shan and S. Y. Choe, "Modeling and simulation of a PEM fuel cell stack considering temperature effects," *J. Power Sources*, vol. 158, pp. 274–286, 2006.

[11] S. Gurski, "Cold start effects on performance and efficiency for vehicle fuel cell system," M.Sc. thesis, Virginia Polytech. Inst. State Univ., Blacksburg, 2002.

[12] Y. M. Feng, Y. C. Tzang, B. S. Pei, C. C. Sun, and A. Su, "Analytical and experimental investigation of a proton exchange membrane fuel cell," *Int. J. Hydrogen Energy*, vol. 29, pp. 381–391, 2004.

[13] M. Wöhr, K. Bolvin, W. Schnurnberger, M. Fischer, W. Neubrand, and G. Eigenberger, "Dynamic modeling and simulation of a polymer membrane fuel cell including mass transport limitation," *Int. J. Hydrogen Energy*, vol. 23, no. 3, pp. 213–218, 1998.

[14] P. C. Krause and O. Wasynczuk, *Electromechanical Motion Devices*, 1st ed.   New York: McGraw-Hill, 1989.

[15] Phoenix Design & Technologies, (Aug. 2006). The PDAT Turbomix [Online]. Available: http://www.padtinc.com/sales/fuelcell/turbomix/

[16] D. G. Kroger, "Radiator characterization and optimization," *SAE Trans.*, vol. 93, pp. 2984–2990, 1984.

[17] R. T. Meyer and B. Yao, "Modeling and simulation of a modern PEM fuel cell system," presented at the ASME Fuel Cell Conf. 2006, Irvine, CA, Jun. 2006.

[18] J. C. Amphlett, R. M. Baumert, R. F. Mann, B. A. Peppley, and P. R. Roberge, "Performance modeling of the Ballard Mark IV solid polymer electrolyte fuel cell," *J. Electrochem. Soc.*, vol. 142, no. 1, pp. 9–15, 1995.

[19] W. J. Choi, P. N. Enjeti, and J. W. Howze, "Development of an equivalent circuit model of a fuel cell to evaluate the effects of inverter ripple current," in *Proc. 19th Annu. IEEE Appl. Power Electron. Conf. Expo. (APEC 2004)*, vol. 1, pp. 355–361.

[20] A. J. Forsyth and S. V. Mollov, "Modeling and control of DC-DC converters," *Power Eng. J.*, vol. 12, no. 5, pp. 229–236, Oct. 1998.

[21] D. Logue and P. T. Krein, "Simulation of electric machinery and power electronics interfacing using ATLAB/SIMULINK," in *Proc. 7th Workshop Comput. Power Electron.*, Jul. 2000, pp. 34–39.

[22] J. Schiffer, O. Bohlen, R. W. De Doncker, D. U. Sauer, and K. Y. Ahn, "Optimized energy management for fuelcell-supercap hybrid electric vehicles," in *Proc. 2005 IEEE Conf. Veh. Power Propulsion*,, Sep. 7–9, pp. 341–348

[23] P. Thounthong, S. Raël, and B. Davat, "Control strategy of fuel cell/supercapacitors hybrid power sources for electric vehicle," *J. Power Source*, vol. 158, pp. 806–814, 2005.

Song-Yul (Ben) Choe received the Ph.D. degree in electrical engineering from the Technical University of Berlin, Berlin, Germany, in 1991.

He was a Program Manager and a Research Professor in the Center for Advanced Vehicular Systems, Mississippi State University, where he was engaged in research on the fuel cell and the advanced intelligent vehicle. He is an Associate professor in the Mechanical Engineering Department, Auburn University, Auburn, AL. From 1996, he was the Director overseeing advanced automotive technology at Hyundai Corporation for five years, where he was engaged in research and development of alternative power trains such as internal combustion engine (ICE) based hybrid systems and polymer electrolyte membrane (PEM) fuel cell systems. He has extensive experience in advanced propulsion systems and associated controls for vehicles. He is the author or coauthor of over 50 published technical papers and reports.

Jong-Woo Ahn received the B.Eng. degree in aeronautical and mechanical engineering in 2002 from Han-Kuk Aviation University, Seoul, Korea, and the M.S. degree from the Department of Mechanical Engineering, Auburn University, Auburn, AL, where he is currently working toward the Ph.D. degree.

His current research interests include the polymer electrolyte membrane (PEM) fuel cell system design and advanced controls.

Jung-Gi Lee (S'02) was born in Jeonju, Korea, in 1975. He received the B.S. degree in control and instrumentation engineering in 2002 from Chonbuk National University, Jeonju, Korea, and the M.S. degree in electronic and electrical engineering in 2004 from Pohang University of Science and Technology (POSTECH), Pohang, Korea, where he is currently working toward the Ph.D. degree.

During 2003, he was engaged in a joint research at Auburn University. His current research interests include control of power electronic converters/system, ac motor control, and fuel cell systems.

Soo-Hyun Baek received the Ph.D. degree in electrical engineering from Han-yang University, Seoul, South Korea, in 1983.

He is currently a Professor at Electrical Engineering Department, Dongguk University, Seoul. Since 1993, he has been served as an Advisor for different agencies of Korean government and Chaired the conference on the Electrical Machinery and Energy Conversion Systems. His current research interests include electrical machinery and power electronic.

Dr. Baek was elected as the President of the Korean Institute of Electrical Engineers Association.